frontiers | Frontiers in Chemistry

TYPE Original Research
PUBLISHED 20 March 2024
DOI 10.3389/fchem.2024.1380551

OPEN ACCESS

EDITED BY
Zijun Bie,
Bengbu Medical College, China

REVIEWED BY
Daojin Li,
Luoyang Normal University, China
Jinliang Zhuang,
Guizhou Normal University, China
Yanting He,
Bengbu Medical College, China

*CORRESPONDENCE
Suhua Fan,
fansuhua@fudan.edu.cn
Hai Wu,
wuhai317@126.com

RECEIVED 01 February 2024
ACCEPTED 11 March 2024
PUBLISHED 20 March 2024

CITATION
Wang L, Zhang M, Li Y, Chen X, Qin H, Yang J, Fan S and Wu H (2024), Construction of porphyrinic manganese-organic frameworks based on structural regulation for electrochemical determination of nitrobenzene in water and vegetable samples.
Front. Chem. 12:1380551.
doi: 10.3389/fchem.2024.1380551

Construction of porphyrinic manganese-organic frameworks based on structural regulation for electrochemical determination of nitrobenzene in water and vegetable samples

Li Wang, Mengjie Zhang, Yuanyuan Li, Xiumei Chen, Hao Qin, Jin Yang, Suhua Fan* and Hai Wu*

Anhui Province Key Laboratory for Degradation and Monitoring of Pollution of the Environment, Anhui Province Key Laboratory of Environmental Hormone and Reproduction, Fuyang Normal University, Fuyang, China

Nitrobenzene (NB) is one of the major organic pollutants that has seriously endangered human health and the environment even in trace amounts. Therefore, it is of great significance to detect trace NB efficiently and sensitively. Herein, a porphyrinic metal-organic framework (MOF) of Mn-PCN-222 (PCN, porous coordination network) was first synthesized by the coordination between Zr_6 cluster and tetrakis (4-carboxyphenyl)-porphyrin-Mn (III) (MnTCPPCl) ligand. To regulate its structure and the electrochemical properties, a phenyl group was inserted in each branched chain of TCPP to form the TCBPP organic ligand. Then, we used Zr_6 clusters and manganese metalloporphyrin (MnTCBPPCl) to synthesize a new porphyrin-based MOF (Mn-CPM-99, CPM, crystalline porous material). Due to the extended chains of TCPP, the rod-shaped structure of Mn-PCN-222 was switched to concave quadrangular bipyramid of Mn-CPM-99. Mn-CPM-99 exhibited higher porosity, larger specific surface area, better electrochemical performances than those of Mn-PCN-222. By using modular assembly technique, Mn-CPM-99 film was sequentially assembled on the surface of indium-tin-oxide (ITO) to prepare an electrochemical sensor (Mn-CPM-99/ITO). The proposed sensor showed excellent electrochemical reduction of NB and displayed three linear response ranges in the wide concentration ranges. The obtained low limit of detection (LOD, 1.3 nM), high sensitivity and selectivity, and good reproducibility of the sensor for NB detection fully illustrate that Mn-CPM-99 is an excellent candidate for electrochemical sensor interface material. Moreover, the sensor was successfully applied to the detection of NB in lake water and vegetable samples showing satisfactory recovery of 98.9%–101.8%.

KEYWORDS

metal-organic frameworks, nitrobenzene, electrochemical sensor, organic pollutants, structural regulation

1 Introduction

Nitrobenzene (NB) and its compounds play crucial roles in the synthesis of dyes, pesticides, and explosives, moreover, they serve as solvents during petroleum refining processes (Li et al., 2022). NB contamination in the environment is mainly from the discharge of industrial waste by chemical plants and dyestuff factories (Wang et al., 2023). Due to its moderate water solubility and higher density relative to water, NB compounds tend to sink to the bottom of water and persist for a prolonged period, resulting in severe and persistent pollution of natural water resources (Lu et al., 2023; Wang et al., 2024). When NB enter into the human body, it can lead to a serious problem of methemoglobinemia and liver cancer and remain carcinogenic activities even at trace level (Fang et al., 2021; Li et al., 2021). Moreover, the presence of a nitro group in NB compounds contributes to their poor biodegradability in electron-deficient environments. The allowable level of NB in all types of water is regulated no more than 2 mg·L^{-1} (16.25 μM) by the World Health Organization (WHO) and American Public Health Association (APHA) (Li et al., 2023). It is therefore imperative to enhance environmental monitoring and research on nitrobenzene compounds, implement stricter emission controls, mitigate environmental pollution, and safeguard human health (Seal et al., 2022; Chellappa et al., 2024).

Various analytical methods including gas chromatography-mass spectrometry (GC-MS) (Zhang et al., 2014), high performance liquid chromatography (HPLC) (Wang and Chen, 2002), spectrophotometry (Rafique et al., 2023; Rahman and Ahmad, 2024) and electrochemical techniques have been used for the detection of NB (Koohfar et al., 2023; Wang et al., 2023; Papavasileiou et al., 2024). Among them, electrochemical techniques have received widespread attention due to their simple operation, high sensitivity, and low cost for detecting nitrobenzene. However, the key of electrochemical sensors is to prepare the interface materials with excellent selectivity and good catalytic performance. Metal-organic frameworks (MOFs) are hybrid materials composed of both organic linkers and inorganic metal nodes, and have been extensively used to construct electrochemical sensors (Kajal et al., 2022). MOFs possess special active sites and many advantages due to their controllable structure, high specific surface area, good stability, and tailored functionalities (Zhang et al., 2023; Junior et al., 2024). The composition of organic and inorganic components can be adjusted to control the structure and performances of MOFs, enhancing their sensing capabilities, e.

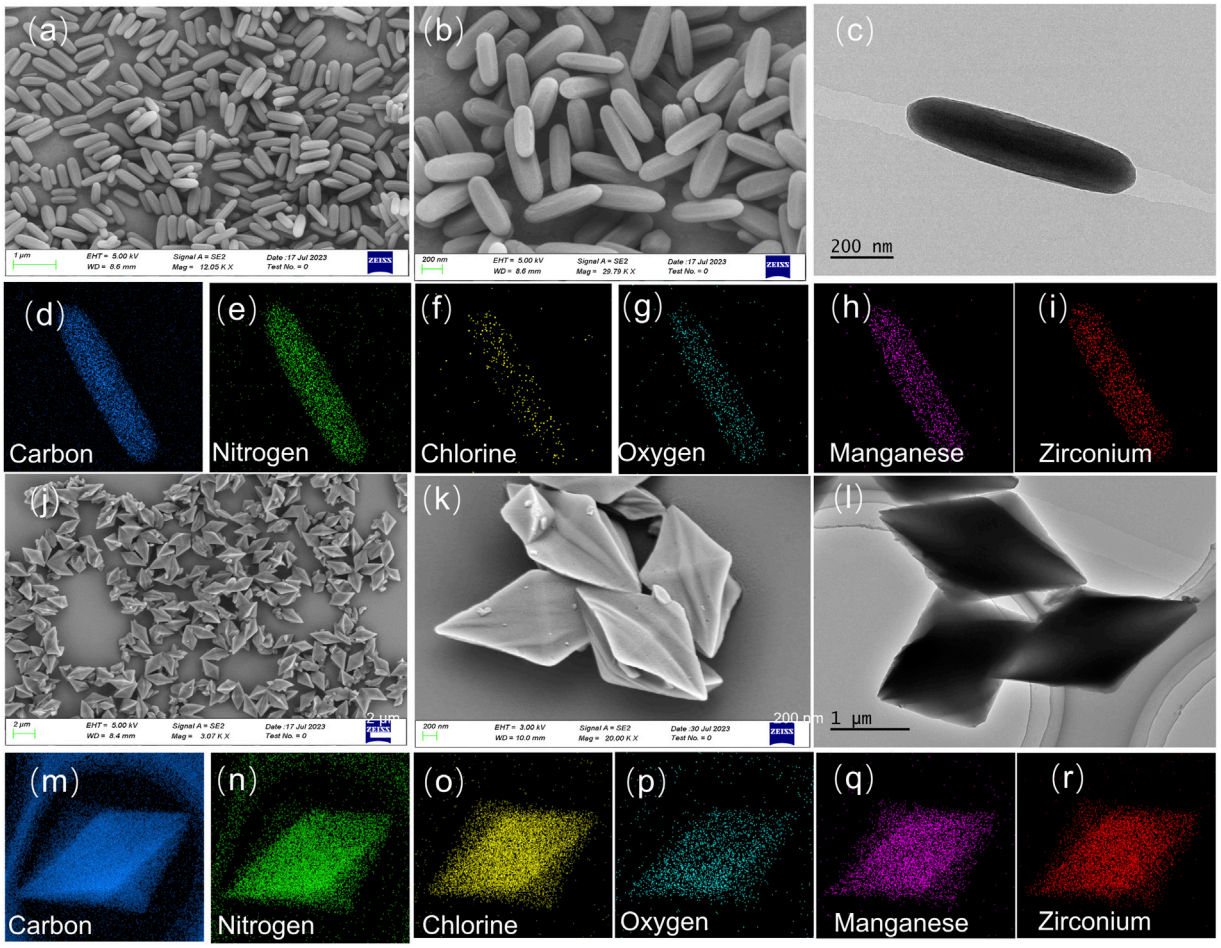

FIGURE 1
SEM images of Mn-PCN-222 **(A,B)** and Mn-CPM-99 **(J,K)**. TEM images of Mn-PCN-222 **(C)** and Mn-CPM-99 **(L)**, respectively. Element mapping images of Mn-PCN-222 **(D–I)** and Mn-CPM-99 **(M–R)**, respectively.

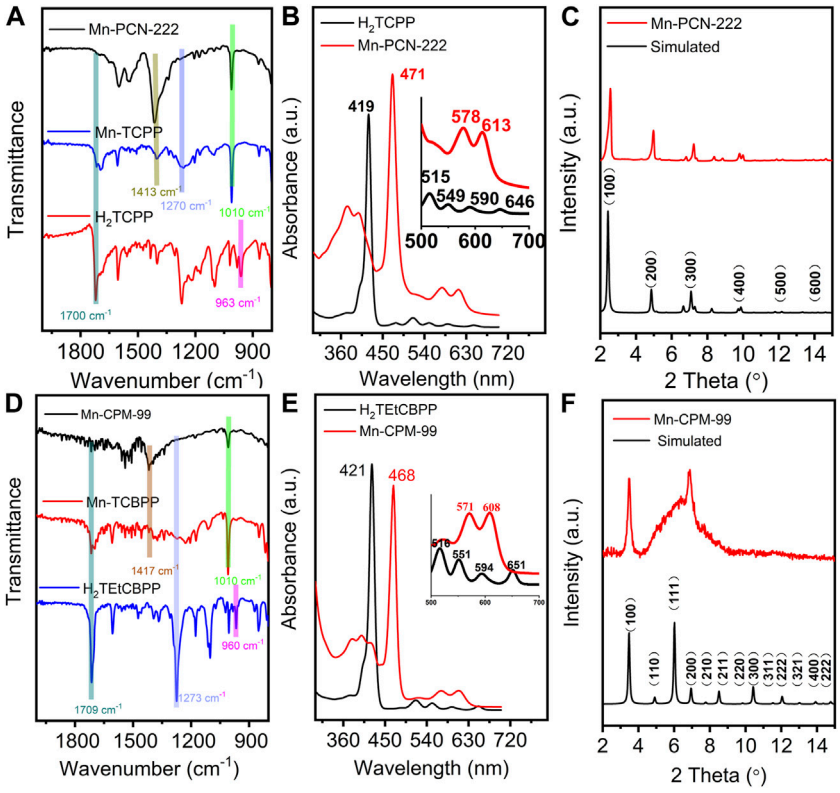

FIGURE 2
(A,D) ATR-IR spectra of free H_2TCPP ligand, MnTCPPCl ligand, Mn-PCN-222, free H_2TEtCBPP ligand, MnTCBPPCl ligand, and Mn-CPM-99. **(B,E)** UV-Vis spectra of free H_2TCPP ligand and Mn-PCN-222 and free H_2TEtCBPP ligand and Mn-CPM-99 (Inset presents a zoomed view of the enlarged Q-band region for clarity). **(C,F)** PXRD patterns of the simulated (red curves) and prepared (blue curves) Mn-PCN-222 and Mn-CPM-99, respectively.

g., by incorporating specific functional groups for target recognition to realize selective detection of target analytes (Liu et al., 2020; Chang et al., 2022). Therefore, several electrochemical sensors based on MOFs have been developed including Cu-MOF (Xin et al., 2023), PCN-222(Fe) (Li et al., 2023), Fe-MOF (Dhayanithi et al., 2023) and showed outstanding sensitivity for the detection of analytes. The adjustable structure and chemical properties make MOFs and their derived materials promising candidates for the development of advanced electrochemical sensors.

Porphyrin-based MOFs can selectively response to NB compounds due to the inherent porphyrin recognition sites in MOFs, exhibiting rapid and selective detection of NB compounds, even in the presence of other interfering compounds (Yang et al., 2015; Zhang et al., 2021). A Zr (IV)-porphyrin MOF PCN-224 (PCN, porous coordination network) was used as fluorescent sensor for rapid detection of 2,4,6-trinitrotoluene (TNT) in aqueous solution (Yang et al., 2015). Fischer et al. proposed an electrochemical sensor using a porphyrin-based MOF (Mn-PCN-222) modified on a conductive indium-tin-oxide (ITO) surface for a variety of electrochemical applications, including nitroaromatics, phenolic and quinone-hydroquinone toxins, heavy metal ions, and biological species (Zhou et al., 2021). The excellent features were attributed to their well-defined porous structures, good electron transfer, and selective reaction between tetra(4-carboxyphenyl)porphyrin (TCPP) and nitroaromatics through hydrogen bonding and π–π stacking interaction.

In this research, to utilize the advantages of porphyrin-based MOFs, we employed Zr_6 clusters as nodes and manganese metalloporphyrin as ligand to prepare a new porphyrin-based MOF (Mn-CPM-99, CPM, crystalline porous material). As shown in Scheme 1A, Zr_6 cluster and Mn-TCPP were first coordinated to construct Mn-PCN-222, containing one of the 1D hexagonal mesoporous channels (Feng et al., 2012; Zhou et al., 2021). To regulate its structure, a phenyl group was inserted in each branched chain of Mn-TCPP to form the Mn-TCBPP ligand, and then, Mn-CPM-99 was prepared. Due to the extended chains of TCPP, the rod-shaped structure of Mn-PCN-222 was switched to quadrangular bipyramid of Mn-CPM-99. Their chemical structures, morphologies, electrochemical behavior, and electrocatalytic abilities were compared in this study. The results showed that the Mn-CPM-99 based electrochemical sensor exhibited high sensitivity and good performances for detection of NB in water and vegetable.

2 Experiments

2.1 Chemicals and reagents

All chemicals and reagents including N,N-Dimethylformamide (DMF), N,N-Diethylformamide (DEF), tetrahydrofuran (THF), were purchased from Energy Chemical (Shanghai, China) and Aladdin Reagent Shanghai Co. Ltd. (China), and directly utilized

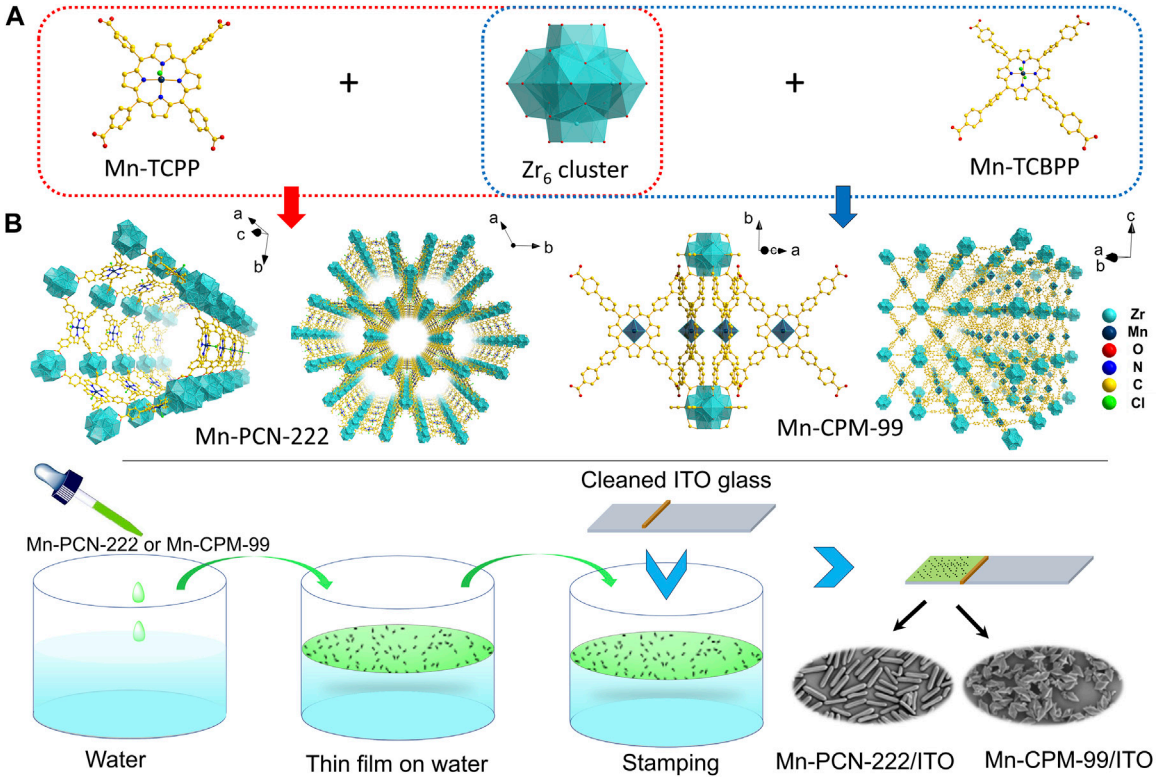

SCHEME 1
(A) Synthesis routs and structures of Mn-PCN-222 and Mn-CPM-99. **(B)** Schematic diagram for the processes of modular assembly of Mn-PCN-222 and Mn-CPM-99 on the ITO electrodes.

without further purification. The synthesis processes and structural characterizations for the Manganese porphyrin Lingands of MnTCPPCl and MnTCBPPCl Ligands were provided in Supplementary Scheme S1; Supplementary Figures S1–S3). Purification of synthesized products was performed on silica gel (300–400 mesh) and self-prepared PTLC (GF254 silica gel).

2.2 Synthesis of Mn-PCN-222 and Mn-CPM-99 MOFs

Mn-PCN-222 was synthesized by a simple one-step solvothermal method (Zhou et al., 2021). $ZrOCl_2$-$8H_2O$ (26 mg), MnTCPPCl (12 mg), and benzoic acid (225 mg) were dissolved in 2 mL of DMF, and ultrasonically dispersed for 10 min. The reaction was then heated with stirring at 80°C and kept for 24 h. When the reaction was cooled to room temperature, the resulting Mn-PCN-222 were rinsed and centrifuged by DMF and ethanol, respectively, and finally dried under vacuum. In the similar way, Mn-CPM-99 were synthesized in DEF solvent at 120°C using 12 mg of MnTCBPPCl ligand.

2.3 Preparation of MOFs film modified ITO electrodes

Mn-PCN-222 and Mn-CPM-99 films was modified on the surface of conductive indium-tin-oxide (ITO) via the modular assembly method. As shown in Scheme 1B, before the modification, the ITO glass was cleaned in ultrasonic baths of acetone, ethanol, and water for 20 min, respectively. Then cleaned ITO was immersed in a solution of (1:1 v/v) ethanol/NaOH (1 M) and was activated for 15 min. Finally, it was rinsed with pure water and dried by N_2. The synthesized Mn-PCN-222 or Mn-CPM-99 were homogeneously dispersed in ethanol with ultrasonication to obtain a colloidal suspension of 1.0 $mg{\cdot}mL^{-1}$, which was dropped onto the water surface in a beaker and then spread out to form a thin film. The film was then transferred onto the cleaned ITO glass by stamping (1 cm × 1 cm). The assembled film was immersed in ultrapure water to remove the un-deposited Mn-PCN-222 or Mn-CPM-99 and then dried by using N_2, Finally, the Mn-PCN-222/ITO and Mn-CPM-99/ITO modified electrodes were obtained.

2.4 Apparatus and measurements

Cyclic voltammetry (CV), chronoamperometric technique (i–t), and electrochemical impedance spectroscopy (EIS) were performed on a CHI660E electrochemical workstation (Chenhua, Shanghai, China). A three-electrode system was used and consisted of a modified ITO electrode as the working electrode (1 cm × 1 cm), a platinum wire served as the auxiliary electrode and an Ag/AgCl electrode (3 M KCl) used as the reference electrode, respectively.

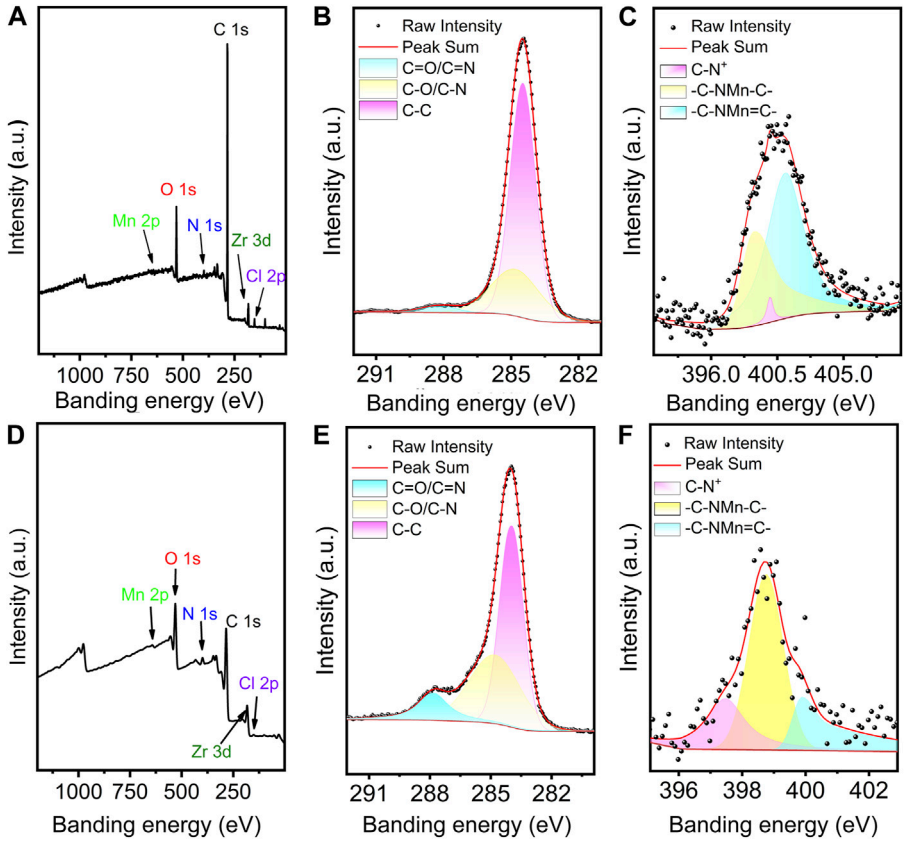

FIGURE 3
Full XPS profiles of Mn-PCN-222 **(A)** and Mn-CPM-99 **(D)**. The high-resolution XPS spectra of C 1s **(B,E)** and N 1s **(C,F)** in Mn-PCN-222 and Mn-PCN-222, respectively.

The morphology, composition, elements, and chemical structure of Mn-PCN-222 and Mn-CPM-99 were characterized by Scanning electron microscope (SEM, Sigma 500, Carl Zeiss, Germany), Transmission electron microscope (TEM, Tecnai G2 F30, FEI, USA), powder X-ray diffraction (XRD, SmartLab SE, Rigaku, Japan), X-ray photoelectron spectroscopy (XPS, K-Alpha, Thermo Scientific, USA), Attenuated total reflectance Infrared spectroscopy (ATR-IR, Nicolet iS50, Thermo Fisher, USA), and UV-Vis spectroscopy (UV-2700i spectrometer, Shimadzu, Japan). ^{1}H NMR spectra for the characterization of the Mn-PCN-222 and Mn-CPM-99 structures in Supplementary Material were measured on a Bruker Ascend 400 MHz instrument (NMR, Ascend 400, BRUKER, Switzerland).

3 Results and discussion

3.1 Characterization of Mn-PCN-222 and Mn-CPM-99

As described in Supplementary Scheme S1, the intermediates of TPPCOOMe and H_2TEtCBPP were synthesized and characterized by ^{1}H NMR spectra, and they were further coordinated with manganese metal ions to obtain MnTCPPCl and MnTCBPPCl ligands, respectively (Supplementary Figures S1–S3). MnTCPPCl and MnTCBPPCl were then hydrolyzed to produce side-chain ester groups, which were then reacted with Zr_6 clusters by solvothermal synthesis method to get the Mn-PCN-222 and Mn-CPM-99 MOFs, respectively. The sizes and morphologies of MnTCPPCl and MnTCBPPCl were observed by SEM and TEM measurements, respectively.

As shown in Figures 1A–C, Mn-PCN-222 presents regular rod shape with an average diameter of 165 nm. However, Mn-CPM-99 exhibits the structure of concave quadrangular bipyramid with uniform distribution (about 700–850 nm long, Figures 1J–L). The Energy-dispersive X-ray spectroscope (EDS) elemental mapping of Mn-PCN-222 and Mn-CPM-99 MOFs were performed to reveal the element distribution. The EDS spectra presented in Supplementary Figure S4 confirm the presence of C, N, Cl, O, Mn, and Zr elements in the samples. We can find that all the measured elements (C, N, Cl, O, Mn, Zr) in the elemental maps are uniformly distributed in the samples (Figures 1D–I; Figures 1M–R). The clean and homogeneous surfaces of Mn-PCN-222 and Mn-CPM-99 MOFs indicate that the synthesis was successful and could obtain relatively pure compounds.

The compositions of Mn-PCN-222 and Mn-CPM-99 were analyzed by attenuated total reflection infrared spectroscopy (ATR-IR) and UV-Vis spectroscopy. As shown in Figure 2A, compared with the free H_2TCPP ligand, MnTCPPCl ligand exhibits a new peak at 1010 cm^{-1} assigned to Mn-N bonds with

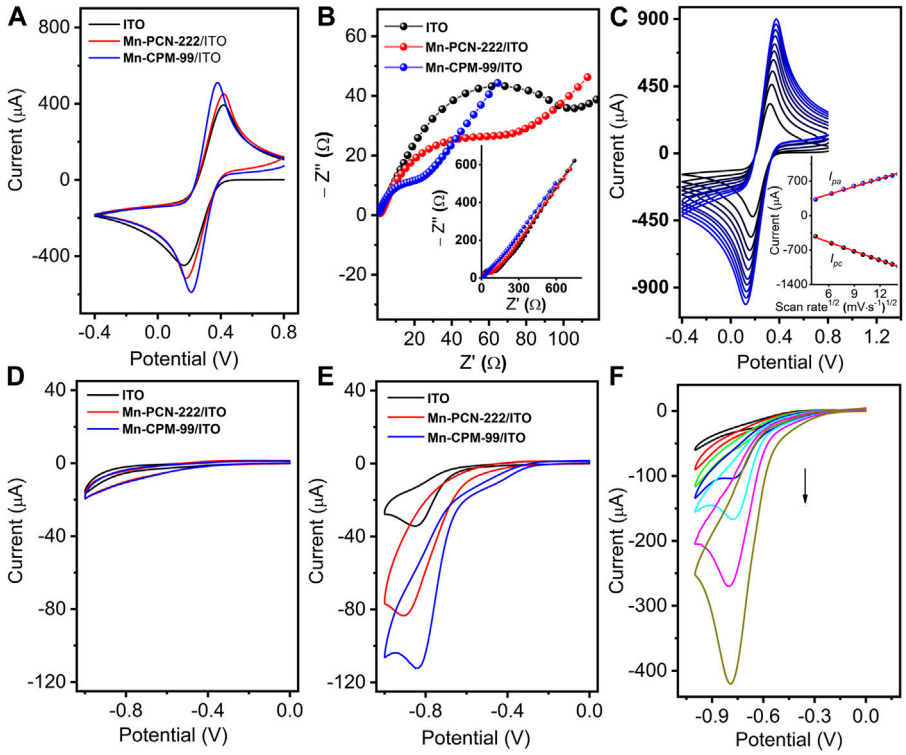

FIGURE 4
(A) CV and **(B)** EIS of ITO, Mn-PCN-222/ITO, and Mn-CPM-99/ITO in 5 mM $[Fe(CN)_6]^{3-/4-}$ solution with 0.1 M KCl (scan rate: 50 mV·s^{-1}). **(C)** CVs of Mn-CPM-99/ITO at different scan rates from 20 to 200 mV·s^{-1} (Inset: The linear relationship between redox peak currents (I_{pa} and I_{pc}) and the square root of the scan rates). **(D,E)** CVs of different modified electrodes in 0.4 M NaCl (pH 7.0) without and with 40 μM NB, respectively. **(F)** CV response of the Mn-CPM-99/ITO sensor in 0.4 M NaCl toward various concentration of NB (0.06, 0.3, 3, 24, 60, 150, and 300 μM).

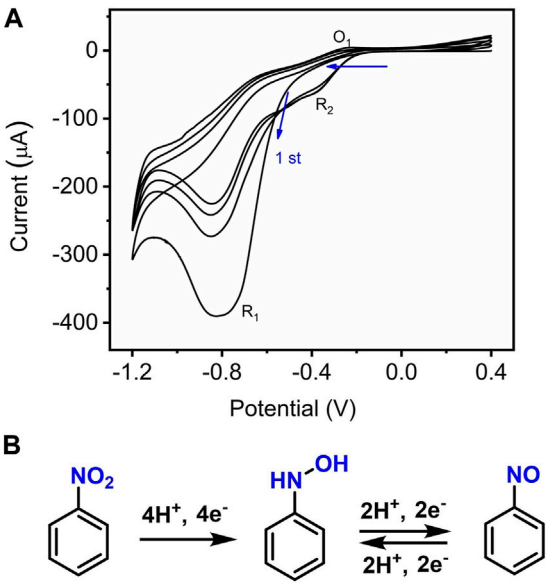

FIGURE 5
(A) CVs of Mn-CPM-99/ITO in 0.4 M NaCl (pH 7.0) containing 0.3 mM NB for four potential cycle scans; **(B)** Electrochemical redox processes of NB on the interface of Mn-CPM-99/ITO.

the disappearance of the N-H stretching vibration peak at 963 cm^{-1}, indicating the coordination of Mn to porphyrin ring in MnTCPPCl (Yu et al., 2020; Xu et al., 2021; Zhou et al., 2021). The signature of Mn-N bonds is also observed in the Mn-PCN-222 film. In contrast to MnTCPPCl, Mn-PCN-222 does not show the characteristic peaks of C=O bonds (1700 cm^{-1}) and C–O bonds (1270 cm^{-1}) whereas exhibits strong peak of –COO symmetric stretch bonds (1413 cm^{-1}), suggesting the carboxyl group coordinating to the Zr_6 centers in MnTCPPCl (Figure 2D). The results are agreement with those in the literature and which suggested the Mn-PCN-222 material was prepared successfully (Zhou et al., 2021). Similarly, the ATR-IR spectra of Mn-CPM-99 does not show the characteristic peaks near 1709 cm^{-1} (C=O bond) and 1273 cm^{-1} (C-O bond) of MnTCBPPCl and H_2TEtCBPP, while the emergence of a strong peak at 1417 cm^{-1} (COO symmetric stretching bond) reflects the carboxyl group coordinated to the Zr_6 cluster in MnTCBPPCl (Zhou et al., 2021; Zhu et al., 2021; Kaur et al., 2023). In addition, the metallation of the MnTCBPPCl ligand can be proved by the disappearance of the N-H stretching vibration at 960 cm^{-1} and the appearance of a new peak for the Mn-N bond at 1010 cm^{-1}. The UV-Vis spectra of both H_2TCPP and H_2TEtCBPP ligands present a strong Soret band and four Q-bands (Figures 2B, E). Furthermore, the Soret bands of Mn-PCN-222 and MnTCBPPCl films are noticed to undergo red shifts about

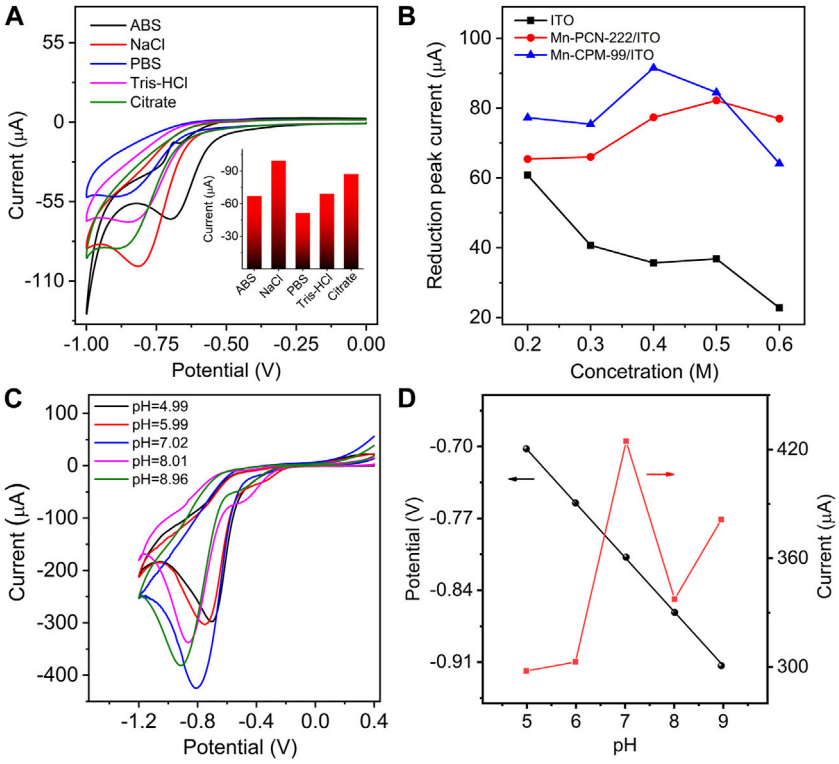

FIGURE 6
(A) CVs of Mn-CPM-99/ITO in different electrolyte solutions in the presence of 40.0 μM NB. (ABS: acetic acid buffer solution, PBS: phosphoric acid buffer solution, Tris-HCl: Tris (hydroxymethyl) aminomethane hydrochloride, Citate: Sodium citrate-citric acid buffer solutions; Concentration of every solution: 0.4 M). Inset: The reduction peak current in different electrolyte solutions. **(B)** The reduction peak currents of NB at different electrodes in NaCl solution with various concentration from 0.20 to 0.60 M **(C)** CVs of Mn-CPM-99/ITO toward 0.30 mM NB of in 0.40 mM NaCl with different pH. **(D)** Change in the reduction peak potential and current at different pH obtained from **(C)**.

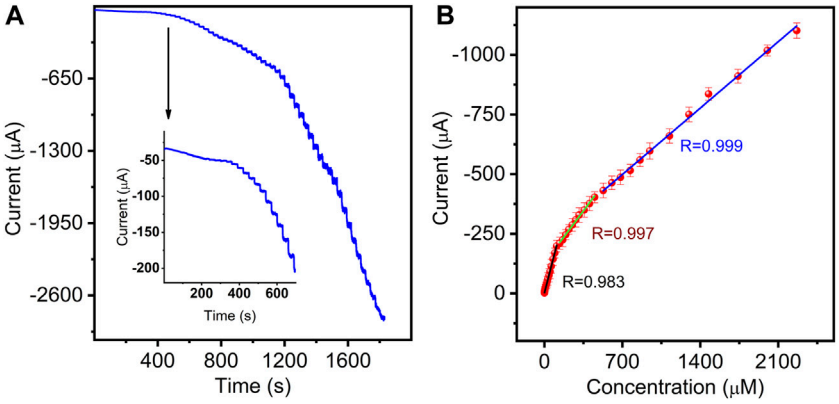

FIGURE 7
(A) Amperometric responses of the sensor in 3.0 mL stirring 0.4 M NaCl aqueous solution with successive additions of NB (0.005–2266 μM). **(B)** Corresponding calibration curves between electrocatalytic currents and NB concentrations (error bars represent standard deviations for three tests).

50 nm, and only two Q bands can be observed, confirming the metalation of porphyrin rings by Mn(III) in the Mn-PCN-222 films. Moreover, there is no characteristic peak of the free TCPP or other new metallized TCPP, indicating the absence of Mn leaching and substitution by other metal ions during the synthesis of Mn-PCN-222 films.

Powder X-ray diffraction (PXRD) patterns of Mn-PCN-222 and Mn-CPM-99 were recorded in Figures 2C, F. The results show that the intense diffraction peaks of Mn-PCN-222 are in good agreement with the simulated XRD profile, which indicate that the three-dimensional Mn-PCN-222 has been successfully prepared. Figure 2F displays the XRD patterns of Mn-CPM-99 which the

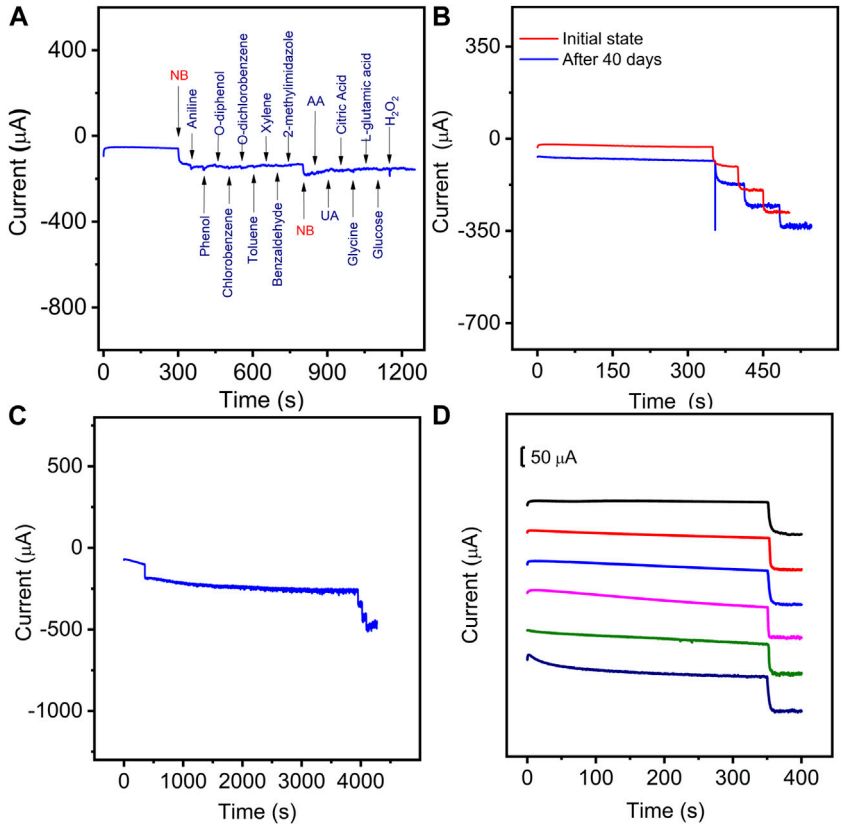

FIGURE 8
(A) Amperometric responses of the Mn-CPM-99/ITO sensor in 3.0 mL stirring 0.4 M NaCl aqueous solution with successive additions of 50.0 μM NB, 200 μM Aniline, phenol, o-diphenol, chlorobenzene, o-dichlorobenzene, Toluene, xylene, benzaldehyde, 2-Methylimidazole, AA, UA, citric acid, Glycine, L-glutamic acid, glucose, and H_2O_2 at the applied potential of −0.8V. **(B)** Storage stability of the Mn-CPM-99/ITO sensor in response to 50.0 μM NB after 40 days. **(C)** Successive current response of the sensor toward 50.0 μM NB before and after 4000 s response. **(D)** The current-time curves of six Mn-CPM-99/ITO electrodes toward 50 μM NB.

TABLE 1 Detection of NB in the real samples.

Samples	Added (μM)	Average detected value (μM)	Average recovery (%)	Mean relative standard deviation (%)
River water	–[a]	–	–	–
	3.00	3.01	100.2	3.17
	6.00	5.93	98.9	3.70
Pakchoi vegetable	–	0.85	–	4.39
	5.00	5.87	100.4	1.16
	10.00	11.03	101.8	0.70

[a]NB, could not be detected.

plane of (100) is located at 2θ of 3.5°. Meanwhile, the broad peak around 2θ of 7° is attributed to the X-ray diffraction peak broadening by amorphization effect. These results indicate the existence of nanocrystals with tiny size in the structure of Mn-CPM-99. More evidences in Supplementary Figure S5 exhibit that Mn-CPM-99 are combined by the nanocrystals sizing of ca. 5.9 nm and organic ligands with disordered structures. Further, the calculated interplanar spacing of the nanocrystals is about 1.28 nm which is corresponding to the plane of (200) locates at 6.94° (Kollias et al., 2022; Xu et al., 2022). Then, the highly dispersed diffraction ring in Supplementary Figure S6 of the selected electron diffraction pattern confirms Mn-CPM-99 possess typical amorphous structure. The abovementioned results are identical to the conclusion of the XRD pattern for Mn-CPM-99.

The elemental valence states of Mn-PCN-222 and Mn-CPM-99 materials were investigated using XPS analysis, respectively. The full XPS survey spectra are shown in Figures 3A, D and demonstrate the presence of the C, N, Cl, O, Mn, and Zr elements in the

Mn-PCN-222 and Mn-CPM-99 materials, which are in good agreement with the above-mentioned results of the EDX energy spectra. In Figure 3B, the three peaks at 288.07 eV, 284.80 eV, and 284.48 eV in the C 1s spectra are attributed to the C-O/C-N, C-C, C=O/C=N valence bonding structure of the TCPP framework, respectively. Correspondingly, the three resolved peaks from the C 1s spectra at 287.81 eV, 284.80 eV and 283.96 eV are attributed to the C-O/C-N, C-C, C=O/C=N valence bond structures of the TCBPP framework, respectively (Figure 3E). Figures 3C, F show the peaks at 399.98, 398.98 and 401.18 eV in Mn-PCN-222 and 397.47, 398.75, and 399.89 eV in Mn-CPM-99 for the N 1s, corresponding to C-N, C-N-Mn-C, and C-N-Mn=C, respectively. Both of the Mn 2P XPS spectra of the Mn-PCN-222 (Supplementary Figure S7A) and Mn-CPM-99 (Supplementary Figure S7B) show four peaks for two oxidation states of Mn(III) and Mn(II) in $2P_{1/2}$ and $2P_{3/2}$ bimodal states, respectively. The amplified spectrum of O 1s (Supplementary Figure S7C, D) can be deconvoluted into three peaks (531.06, 532.3 and 529.65 eV in Mn-PCN-222; 532.5, 531.9 and 530.37 eV in Mn-CPM-99), which are attributed to the C=O, Zr-O, and C-O valence bond structures, respectively. These results confirm the successful preparation of Mn-PCN-222 and Mn-CPM-99.

3.2 Electrochemical properties of the different modified electrodes

Mn-PCN-222 and Mn-CPM-99 were rapidly integrated on ITO glass by modular assembly method to obtain the Mn-PCN-222/ITO and Mn-CPM-99/ITO modified electrodes, which were characterized by CV technology and electrochemical impedance method. The CV curves of the ITO, Mn-PCN-222/ITO, and Mn-CPM-99/ITO electrodes were recorded in 5 mM $[Fe(CN)_6]^{3-/4-}$ solution with 0.1 M KCl at a scan rate of 50 $mV{\cdot}s^{-1}$ (Figure 4A). Compared to the ITO and Mn-PCN-222/ITO electrodes, the Mn-CPM-99/ITO electrode shows the best reversible redox peaks and largest peak currents. All their corresponding Nyquist plots in 5 mM $[Fe(CN)_6]^{3-/4-}$ solution Figure 4B show very small resistivity (R_{ct}). But the R_{ct} value of the Mn-CPM-99/ITO electrode (34 Ω) is significantly lower than those of Mn-PCN-222/ITO (86 Ω) and ITO (124 Ω). The results can be attributed to the strong synergistic effect between the organic ligand and the zirconium clusters after ring extension, resulting in more active sites, lower charge transfer resistance, and a larger contact area between the electrode and electrolyte. The CV curves of the Mn-CPM-99/ITO, ITO, and Mn-PCN-222/ITO electrodes at different scan rates (20–200 $mV{\cdot}s^{-1}$) are shown in Figure 4C and Supplementary Figure S8. There are good linear relationships between the redox peak currents and the square root of the scan rates. The good linearity indicates that the redox process of the $[Fe(CN)_6]^{3-/4-}$ probe is a diffusion-controlled process at the modified electrodes. According to the Randles-Sevcik equation (Supplementary Figure S8), the electrochemically active surface areas of ITO, Mn-PCN-222/ITO and Mn-CPM-99/ITO were calculated to be 0.353, 0.497, and 0.558 cm^2, respectively, and therefore, the significantly larger active surface area of Mn-CPM-99/ITO provides obvious advantages for NB detection.

To investigate the catalytic activities, the CV responses of the modified electrodes were recorded in 0.4 M NaCl. As shown in Figure 4D, in the absence of NB, three different electrodes do not show obvious reduction peaks, but show different capacitive characteristics from ITO, Mn-PCN-222/ITO, and Mn-CPM-99/ITO modified electrodes due to their porosity and specific surface area. In the presence of NB, Mn-CPM-99/ITO shows sharp and well-defined reduction peak with the highest peak currents and more positive reduction potentials compared to other modified and unmodified electrodes (Figure 4E). Based on the special structure of the manganese metal porphyrin-based MOFs, the higher electrocatalytic activity for NB can be ascribed to reasons as follows: Firstly, the highly conjugated porphyrin ring (π–π stacking interaction with the NB molecules) and the large specific surface of Mn-PCN-222 and Mn-CPM-99 as the porous substrates enable the sensor interface to effectively trap NB molecules; Secondly, the inherent redox activity of the organic ligands TCPP and TCBPP, and the reduction of the electron intermediate of Mn(III) to Mn(II) state in the center of Mn-PCN-222 and Mn-CPM-99 structure contribute to the acceleration of electron transport, which were confirmed by the electrocatalysis of NB on TCPP/ITO, TCBPP/ITO, MnTCPP/ITO, and MnTCBPP/ITO electrodes (Supplementary Figure S9). In addition, the strong electron-withdrawing property of NB itself leads to the formation of an electron donor-acceptor (EDA) system between the porphyrin centers, which facilitates the transfer of electrons to the nitrobenzene, causing its protonation and ultimately leading to the reduction of NB (Zhou et al., 2021).

Figure 4F shows a typical CV response of the Mn-CPM-99/ITO sensor upon continuous addition of NB in 0.4 M NaCl solution. The dramatic increase in the reduction peak currents of NB suggested that the presented sensor showed typical electrocatalytic reduction of NB. In order to study the electrochemical process, CV of 0.5 mM NB was continuously scanned with a wider potential range between 0.4 V and −1.2 V (Figure 5A). During the first sweep, CV of NB at Mn-CPM-99/ITO presents only an irreversible cathodic peak (R_1) at −0.8 V, which is related to the $4H^+/4e^-$ reduction of the nitro group ($-NO_2$) in NB to phenylhydroxylamine. Starting from the second cycle scan, the reduction peak at −0.83 V gradually decreases, and a pair of new redox peaks (O_1/R_2) gradually appear and increase between −0.2 V and −0.4 V, which corresponds to is the $2H^+/2e^-$ redox process between phenylhydroxylamine and nitrosobenzene (Li et al., 2023; Yuan et al., 2023). The results suggested that phenylhydroxylamine was gradually produced by electrochemical reduction of NB, and then was oxidized to nitrosobenzene, appearing a new reduction peak (R_2). The overall redox mechanism of NB is summarized in Figure 5B.

3.3 Effect of the electrolyte solutions and pH

To achieve the best electrochemical response, the effects of different electrolyte solutions, electrolyte concentration, and pH of the solution on the electrocatalysis of the sensor toward NB were investigated (Sang et al., 2014; Stergiou et al., 2022). In different electrolyte and buffer solutions, the best response of the Mn-CPM-99/ITO electrode toward NB was obtained in NaCl solution (Figure 6A and inset). Figure 6B and Supplementary

Figure S10 show the electrochemical reduction of 40 μM NB in NaCl solution with various concentrations from 0.2 M to 0.6 M. Obviously, the maximum current of NB could be obtained in 0.4 M NaCl solution. Therefore, 0.4 M NaCl solution was chose as an electrolyte concentration in the following study.

Figure 6C shows the dependence of the sensor on pH. The reduction peak potential shifted negatively with increasing pH. The maximum electrocatalytic current was observed at pH seven and a good linear relationship between peak potential and pH was obtained: Ep (V) = −0.0529 pH−0.438 (Figure 6D). The slope of −0.0529 V/pH is very close to the theoretical value of 0.059 V/pH. The result indicates that an equal number of electrons and protons is involved in the NB electrochemical reduction process (Yuan et al., 2023), which is consistent with the proposed redox mechanism of NB in Figure 5B. All the electrochemical results suggest that Mn-CPM-99/ITO has better response sensitivity to NB and it is more suitable as an electrochemical sensor for detecting NB in aqueous solution.

3.4 Amperometric (i-t) determination of NB on Mn-CPM-99/ITO

To obtain higher response sensitivity, the chronoamperometric technique was performed. As shown in Figure 7A, upon successive addition of different concentrations of NB into stirred solution, the sensor exhibited rapid and typical amperometric current response to NB at the applied potential of −0.77 V. The inset of Figure 7A shows a magnified plot of the reduced current response at low NB concentration. The reduction peak currents grew linearly with the increase in three NB concentration ranges from 5 nM to 109.5 μM, 136.7–450.2 μM, and 527.5–2266 μM (Figure 7B) with the corresponding sensitivities of 1.817 (R = 0.983), 0.621 (R = 0.997), and 0.398 μA μM^{-1} (R = 0.999), respectively. Obviously, at low concentration, the sensor showed higher sensitivity for NB determination due to more available catalytic sites. The limit of detection (LOD) was calculated as low as 1.3 nM (Wu et al., 2018), which is lower than the permissible limit in water (16.25 μM) regulated by APHA (Li et al., 2023). The analytical performances are comparable with those in previously reported NB sensors (Supplementary Table S1).

3.5 Analytical performance of the proposed sensor

The selectivity of the presented sensor towards Nb was first evaluated by adding 4-fold interfering substances using the amperometric (*i-t*) method. As shown in Figure 8A, the current responses on NB were not interfered by the injection of the common organics (aniline, phenol, o-diphenol, chlorobenzene, o-dichlorobenzene, toluene, xylene, benzaldehyde, 2-methylimidazole), biomolecules (ascorbic acid (AA), uric acid (UA), citric acid, glycine (Gly), L-glutamic acid (L-GAA), glucose (Glu), and hydrogen peroxide (H_2O_2). Some common cations in aqueous solution were also evaluated including K^+, Na^+, Ca^{2+}, Mg^{2+}, Fe^{2+}, Ni^{2+}, Fe^{3+}, and Cr^{3+} (Supplementary Figure S11). The current response of the interfering metal cations is obviously lower than that of NB at the same concentration level. These results indicate that the proposed sensor has good selectivity for NB detection.

The repeatability and stability reveal the potential capabilities of the proposed method for practical applications. The long-term storage stability of the sensor was evaluated by measuring the response currents of NB for 40 days of storage (Figure 8B), which showed that all the current responses towards three concentrations of NB retained over 97% of their original currents. In Figure 8C, the catalytic current of 50 μM NB does not decay for 4000 s of successive response, furthermore, the sensor still shows a sensitive response to NB, indicating good operational stability. The reproducibility of the sensor was evaluated by utilizing six modified electrodes on different GCEs. As shown in Figure 8D, the relative standard deviations were calculated to be 3.4%, indicating high reproducibility. Therefore, the satisfactory stability and reproducibility suggest that Mn-CPM-99/ITO is potentially applicable as a reliable sensor for the determination of NB in real water samples.

3.6 Analysis of real samples

The practicality of the Mn-CPM-99/ITO electrode was verified by the determination of NB in river water and vegetable (Pakchoi) samples. The Pakchoi vegetable was sprayed with 5 mL 20 mM NB solution. After 1 day, 3 g of fresh leaves were grinded and dissolved in 10 mL ethanol, which was then centrifuged at 6000 rpm. The obtained supernatant of vegetable and river water were filtered through 0.22 μm membrane filter and used directly for the actual sample analysis by standard addition method (Supplementary Figure S12). As shown in Table 1, NB in river water could not be detected while an average of 0.85 μM NB could be detected in the NB-pretreated vegetable samples. All of the recoveries with the added NB standard solution ranged from 98.8% to 101.8%, indicating that the electrochemical sensor based on Mn-CPM-99 MOF has good utility for the determination of NB content in real water or vegetables.

4 Conclusion

In conclusion, a concave quadrangular bipyramidal Mn-CPM-99 MOF was successfully designed based on the coordination reaction between MnTCBPPCl organic ligands and Zr_6 clusters. The structure and electrochemical properties of Mn-CPM-99 MOF were compared with those of Mn-PCN-222 MOF with rod-shaped structure (constructed form TCPP and Zr_6). Due to the broadened chain of TCPP organic ligands by the phenyl group, Mn-CPM-99 MOF shows the bipyramidal structure with higher porosity and larger specific surface area than those of Mn-PCN-222. After comparing their morphology, electrochemical behavior, and electrocatalytic ability, it is found that Mn-CPM-99 modified ITO electrode has better electrocatalytic performances towards NB reduction. The high sensitivity and selectivity, low LOD, wide linear concentration range, and good reproducibility make the presented sensor (Mn-CPM-99/ITO) successfully applied to the detection of NB in river water and vegetable samples. Therefore, the strategy based on the structural design will broaden the

application of the porphyrin-based MOF materials and provide a new platform to study the relationship between structural improvement and its function.

Data availability statement

The original contributions presented in the study are included in the article/Supplementary Material, further inquiries can be directed to the corresponding authors.

Author contributions

LW: Formal Analysis, Investigation, Writing–original draft. Mengjie Zhang: Formal Analysis, Investigation, Writing–original draft. YL: Formal Analysis, Investigation, Writing–original draft. XC: Formal Analysis, Investigation, Writing–original draft. HQ: Formal Analysis, Resources, Writing–review and editing. JY: Investigation, Resources, Writing–review and editing. SF: Conceptualization, Funding acquisition, Software, Writing–review and editing. HW: Funding acquisition, Writing–original draft, Writing–review and editing.

Funding

The author(s) declare financial support was received for the research, authorship, and/or publication of this article. This work was supported by the Natural Science Foundation of Higher Education Institutions in Anhui Province [Nos: 2022AH040201, KJ2021ZD0074, 2023AH050401], the Natural Science Foundation of Anhui Province [No: 2108085MB65], the National and Anhui Province Training Programs of Innovation and Entrepreneurship for Undergraduates [Nos: 202310371040, 202210371015], the Key Projects of Fuyang Normal University for Young Talents [rcxm202212], the Scientific Research and Innovation Team of Fuyang Normal University [No: kytd202001]; the open subject of the provincial research platform inf Fuyang Normal University (FSKFKT018D), and the Horizontal Cooperation Project of Fuyang Municipal Government and Fuyang Normal University [No: SXHZ202010].

Conflict of interest

The authors declare that the research was conducted in the absence of any commercial or financial relationships that could be construed as a potential conflict of interest.

Publisher's note

All claims expressed in this article are solely those of the authors and do not necessarily represent those of their affiliated organizations, or those of the publisher, the editors and the reviewers. Any product that may be evaluated in this article, or claim that may be made by its manufacturer, is not guaranteed or endorsed by the publisher.

Supplementary material

The Supplementary Material for this article can be found online at: https://www.frontiersin.org/articles/10.3389/fchem.2024.1380551/full#supplementary-material

References

Bindu, P., and Thomas, S. (2014). Estimation of lattice strain in ZnO nanoparticles: X-ray peak profile analysis. *J. Theor.* 8, 123–134. doi:10.1007/s40094-014-0141-9

Chang, Y., Lou, J. X., Yang, L. Y., Liu, M. M., Xia, N., and Liu, L. (2022). Design and application of electrochemical sensors with metal–organic frameworks as the electrode materials or signal tags. *Nanomater* 12, 3248. doi:10.3390/nano12183248

Chellappa, V., Meenakshisundaram, N., Annaraj, J., and Sagadevan, S. (2024). Hydrothermal synthesis of MnO_2 nanorods for efficient electrochemical detection of environmental anthropogenic pollutants and nitrobenzene. *Inorg. Chem. Commun.* 160, 112015. doi:10.1016/j.inoche.2023.112015

Chen, X., Feng, X. Z., Zhan, T., Xue, Y. T., Li, H. X., Han, G. C., et al. (2023). Construction of a portable enzyme-free electrochemical glucose detection system based on the synergistic interaction of Cu-MOF and PtNPs. *Sens. Actuators B Chem.* 395, 134498. doi:10.1016/j.snb.2023.134498

Dhayanithi, C. A., Palpandi, K., Raman, N., and Babu, S. G. (2023). Development of amine-based transition metal MOFs as efficient electrochemical sensors for the detection of chloramphenicol in food and pharmaceutical samples. *Electrochim. Acta* 470, 143358. doi:10.1016/j.electacta.2023.143358

Fang, Y., Wang, D., Lv, X., Xu, X., Zhou, H., Liu, P., et al. (2021). Simultaneous electrochemical determination of nitrophenol isomers Based on spirofluorene - based microporous polymer film modified electrodes through one-step electropolymerization strategy. *Sens. Actuators B Chem.* 333, 129568. doi:10.1016/j.snb.2021.129568

Feng, D., Gu, Z., Li, J., Jiang, H., Wei, Z., and Zhou, H. (2012). Zirconium-metalloporphyrin PCN-222: mesoporous metal-organic frameworks with ultrahigh stability as biomimetic catalysts. *Angew. Chem. Int. Ed.* 124, 10453–10456. doi:10.1002/ange.201204475

Junior, D. W., Hryniewicz, B. M., and Kubota, L. T. (2024). Advanced hybrid materials in electrochemical sensors: combining MOFs and conducting polymers for environmental monitoring. *Chemosphere* 352, 141479. doi:10.1016/j.chemosphere.2024.141479

Kajal, N., Singh, V., Gupta, R., and Gautam, S. (2022). Metal organic frameworks for electrochemical sensor applications: a review. *Environ. Res.* 204, 112320. doi:10.1016/j.envres.2021.112320

Kaur, G., Anthwal, A., Kandwal, P., and Sud, D. (2023). Mechanochemical synthesis and theoretical investigations of Fe (II) based MOF containing 4, 4′-bipyridine with ordained intercalated p-aminobenzoic acid: application as fluoroprobe for detection of carbonyl group. *Inorg. Chim. Acta* 545, 121248. doi:10.1016/j.ica.2022.121248

Kollias, L., Rousseau, R., Glezakou, V. A., and Salvalaglio, M. (2022). Understanding metal–organic framework nucleation from a solution with evolving graphs. *J. Am. Chem. Soc.* 144, 11099–11109. doi:10.1021/jacs.1c13508

Koohfar, S., Ghasemi, M., Hafen, T., Dimitrakopoulos, G., Kim, D., Pike, J., et al. (2023). Improvement of oxygen reduction activity and stability on a perovskite oxide surface by electrochemical potential. *Nat. Commun.* 14, 7203. doi:10.1038/s41467-023-42462-5

Li, S., Fang, J., Li, L., Zhu, M., Zhang, F., Zhang, B., et al. (2021). An ultra-sensitive electrochemical sensor of Ni/Fe-LDH toward nitrobenzene with the assistance of surface functionalization engineering. *Talanta* 225, 122087. doi:10.1016/j.talanta.2021.122087

Li, W., Zhao, J., Yan, C., Dong, B., Zhang, Y., Li, W., et al. (2022). Asymmetric activation of the nitro group over a Ag/graphene heterointerface to boost highly selective electrocatalytic reduction of nitrobenzene. *ACS Appl. Mat. Interfaces* 14, 25478–25489. doi:10.1021/acsami.2c04533

Li, Y., Zhuge, R., and Zhang, T. (2023). MOF-conductive polymer composite electrode as electrochemical sensor of nitrobenzene. *Inorg. Chem. Commun.* 154, 110904. doi:10.1016/j.inoche.2023.110904

Lin, Q., Bu, X., Kong, A., Mao, C., Zhao, X., Bu, F., et al. (2015). New heterometallic zirconium metalloporphyrin frameworks and their heteroatom-activated high-surface-area carbon derivatives. *J. Am. Chem. Soc.* 137, 2235–2238. doi:10.1021/jacs.5b00076

Liu, C. S., Li, J. J., and Pang, H. (2020). Metal-organic framework-based materials as an emerging platform for advanced electrochemical sensing. *Coord. Chem. Rev.* 410, 213222. doi:10.1016/j.ccr.2020.213222

Lu, A., Xiang, X., Lei, M., Huang, S., Liang, B., Zhao, S., et al. (2023). Highly efficient catalytic transfer hydrogenation for the conversion of nitrobenzene to aniline over PdO/TiO_2: the key role of *in situ* switching from PdO to Pd. *J. Environ. Sci.* 148, 515–528. doi:10.1016/j.jes.2023.10.010

Papavasileiou, A. V., Antonatos, N., Luxa, J., Dekanovský, L., Ashtiani, S., Fomekong, R. L., et al. (2024). Two-dimensional VSe_2 nanoflakes as a promising sensing electrocatalyst for nitrobenzene determination in water samples. *Electrochim. Acta* 475, 143653. doi:10.1016/j.electacta.2023.143653

Rafique, S., Irshad, H., Majeed, S., Rubab, R., Imran, M., Khan, A. M., et al. (2023). AIEE active stilbene based fluorescent sensor with red-shifted emission for vapor phase detection of nitrobenzene and moisture sensing. *J. Photochem. Photobiol. A* 437, 114459. doi:10.1016/j.jphotochem.2022.114459

Rahman, N., and Ahmad, I. (2024). Coordination polymer gel mediated spectrophotometric, ICP-AES and spectrofluorimetric methods for trace As(III) determination in water and food samples. *Chemosphere* 351, 141272. doi:10.1016/j.chemosphere.2024.141272

Sang, Y. T., Wang, B. Y., Wang, Q. C., Zhao, G., and Guo, P. Z. (2014). Insights into the electrocatalysis of nitrobenzene using chemically-modified carbon nanotube electrodes. *Sci. Rep.* 4, 6321. doi:10.1038/srep06321

Seal, K., Chaudhuri, H., Pal, S., Srivastava, R. R., and Soldatova, E. (2022). A study on water pollution scenario of the Damodar river basin, India: assessment of potential health risk using long term database (1980–2019) and statistical analysis. *Environ. Sci. Pollut. Res.* 29, 53320–53352. doi:10.1007/s11356-022-19402-9

Stergiou, A. D., Broadhurst, D. H., and Symes, M. D. (2022). Electrochemical reduction of nitrobenzene via redox-mediated chronoamperometry. *Star. Protoc.* 3, 101817. doi:10.1016/j.xpro.2022.101817

Wang, K., Zhao, J., Zhang, X., Jiang, L., Zhou, X., Xie, C., et al. (2023). Fluorescent noncovalent organic framework for supporting gold nanoparticles as heterogeneous catalyst with merits of easy detection and recycle. *Small* 20, e2303834. doi:10.1002/smll.202303834

Wang, S., and Chen, H. (2002). Separation and determination of nitrobenzenes by micellar electrokinetic chromatography and high-performance liquid chromatography. *J. Chromatogr. A* 979, 439–446. doi:10.1016/s0021-9673(02)01435-8

Wang, W., Wang, Y., Zhao, X., Li, Y., He, H., Lian, L., et al. (2024). Surface oxygen vacancies of TiO_2–x enabled water transfer photocatalytic hydrogenation of nitrobenzene to aniline without use of co-catalyst. *Chem. Eng. Sci.* 285, 119645. doi:10.1016/j.ces.2023.119645

Wang, X., Guo, A., Fu, Y., Tan, M., Luo, W., and Yang, W. (2023). Porphyrin-conjugated microporous polymer nanospheres as electrocatalysts for nitrobenzene detection and oxygen evolution reaction. *ACS Appl. Nano Mat.* 6, 3226–3235. doi:10.1021/acsanm.2c04811

Weidenthaler, C. (2011). Pitfalls in the characterization of nanoporous and nanosized materials. *Nanoscale* 3, 792–810. doi:10.1039/c0nr00561d

Wu, H., Li, X., Chen, M., Wang, C., Wei, T., Zhang, H., et al. (2018). A nanohybrid based on porphyrin dye functionalized graphene oxide for the application in non-enzymatic electrochemical sensor. *Electrochim. Acta* 259, 355–364. doi:10.1016/j.electacta.2017.10.122

Xu, J., Li, W., Liu, W., Jing, J., Zhang, K., Liu, L., et al. (2022). Efficient photocatalytic hydrogen and oxygen evolution by side-group engineered benzodiimidazole oligomers with strong built-in electric fields and short-range crystallinity. *Angew. Chem. Int. Ed.* 61, e202212243. doi:10.1002/anie.202212243

Xu, Q. B., Zhan, G. T., Zhang, Z. L., Yong, T. Y., Yang, X. L., and Gan, L. (2021). Manganese porphyrin-based metal-organic framework for synergistic sonodynamic therapy and ferroptosis in hypoxic tumors. *Theranostics* 11, 1937–1952. doi:10.7150/thno.45511

Yang, J., Wang, Z., Hu, K. L., Li, Y. S., Feng, J. F., Shi, J. L., et al. (2015). Rapid and specific aqueous-phase detection of nitroaromatic explosives with inherent porphyrin recognition sites in metal–organic frameworks. *ACS Appl. Mat. Interfaces* 7, 11956–11964. doi:10.1021/acsami.5b01946

Yu, K., Puthiaraj, P., and Ahn, W. S. (2020). One-pot catalytic transformation of olefins into cyclic carbonates over an imidazolium bromide-functionalized Mn(III)-porphyrin metal–organic framework. *Appl. Catal. B Environ.* 273, 119059. doi:10.1016/j.apcatb.2020.119059

Yuan, C., Li, N., Zhang, X., Wang, Y., Zhou, S., Zhang, L., et al. (2023). Flower-like copper sulfide-decorated boron-nitrogen co-doped carbon-modified glassy carbon electrode for selective and sensitive electrochemical detection of nitrobenzene in natural water. *Colloids Surf. A-Physicochem. Eng. Asp.* 675, 132011. doi:10.1016/j.colsurfa.2023.132011

Zhang, G., Zhou, X., Zang, X., Li, Z., Wang, C., and Wang, Z. (2014). Analysis of nitrobenzene compounds in water and soil samples by graphene composite-based solid-phase microextraction coupled with gas chromatography–mass spectrometry. *Chin. Chem. Lett.* 25, 1449–1454. doi:10.1016/j.cclet.2014.05.049

Zhang, W. Q., Li, X. J., Ding, X. M., Hua, K., Sun, A., Hu, X. X., et al. (2023). Progress and opportunities for metal–organic framework composites in electrochemical sensors. *RSC Adv.* 13, 10800–10817. doi:10.1039/d3ra00966a

Zhang, X., Wasson, M. C., Shayan, M., Berdichevsky, E. K., Ricardo-Noordberg, J., Singh, Z., et al. (2021). A historical perspective on porphyrin-based metal–organic frameworks and their applications. *Coord. Chem. Rev.* 429, 213615. doi:10.1016/j.ccr.2020.213615

Zhou, Z. Y., Mukherjee, S., Hou, S. J., Li, W. J., Elsner, M., and Fischer, R. (2021). Porphyrinic MOF film for multifaceted electrochemical sensing. *Angew. Chem. Int. Ed.* 60, 20551–20557. doi:10.1002/anie.202107860

Zhu, Y., Zhang, Z., Cheng, J., Guo, H., and Yang, W. J. (2021). Ni-BTC metal-organic framework loaded on MCM-41 to promote hydrodeoxygenation and hydrocracking in jet biofuel production. *J. Hydrogen Energy* 46, 3898–3908. doi:10.1016/j.ijhydene.2020.10.216